Planetary and Space Science 251 (2024) 105958

Contents lists available at ScienceDirect

Planetary and Space Science

journal homepage: www.elsevier.com/locate/pss

About the improvement in Mars Polar Motion determination from radio tracking of two landers

Marta Goli [a,b,*], Sébastien Le Maistre [a,b], Marie Yseboodt [a]

[a] Royal Observatory of Belgium, Avenue circulaire 3, 1180 Brussels, Belgium
[b] Université catholique de Louvain, Place de l'Université 1, 1348 Ottignies-Louvain-la-Neuve, Belgium

ARTICLE INFO

Keywords:
Radio science
Mars
Polar motion

ABSTRACT

The polar motion of Mars is defined as the movement of the rotation axis with respect to a body-fixed frame tied to the crust of the planet. It is composed of forced motion at annual and sub-annual frequencies caused by the seasonal mass redistribution, formation of the polar ice caps and angular momentum variations of the atmosphere, and of the free mode called the Chandler wobble.

Radio-tracking data from landers offers the most suitable means to measure the rotation of Mars, including its polar motion. The latter, however, has not yet been achieved using lander data alone. In this study, we assess the uncertainties associated with Mars polar motion estimation using Direct-To-Earth Doppler, range and Same-Beam Interferometry (SBI) observables between multiple landers on the surface of Mars. We evaluate the improvement enabled by combining data from multiple landers with respect to one-lander scenarios, and identify the optimal mission architectures for polar motion estimation by considering the influence of respective mission parameters on the estimation uncertainty. In particular, we consider the effects of absolute and relative locations of the landers and of mission scheduling. We re-evaluate the possibility of estimating the polar motion using data from landers in proximity to the equator, and apply our considerations to simulated data consistent in number and accuracy with that collected by past Martian missions. We notice and explain a strong longitude dependence of the formal errors when the polar motion parameters are estimated concurrently with the seasonal spin variation parameters, making it impossible to properly determine all components of polar motion with a single lander regardless of its location. However, the use of two or more landers in optimal locations with respect to each other eliminates those limitations. We evaluate the influence of latitudinal and longitudinal separation on polar motion determination in such cases. In particular, we are able to determine polar motion well even in cases where the longitudes of the two landers make determination from each single lander impossible.

1. Introduction

Knowledge of the rotation and orientation of Mars provides useful inputs to models of its interior structure and atmospheric dynamics. Mars rotational motion is customarily described using the precession, nutation, spin, and polar motion angles (Folkner et al., 1997). Those can be obtained using radio science data from landers and orbiters, most commonly using two-way Doppler shift measurements (e.g. Konopliv et al., 2020). Most recently, data from the RISE instrument onboard the InSight lander has been used to improve the Mars rotation, orientation and interior structure models (Le Maistre et al., 2023). In synergy with RISE, the LaRa instrument (Dehant et al., 2020; Le Maistre et al., 2022) developed at the Royal Observatory of Belgium and part of the now-cancelled ExoMars 2022 joint ESA-Roscosmos mission would have provided further constraints on Mars rotation and Orientation Parameters (MOP) (Péters et al., 2020). Unfortunately, LaRa has recently been descoped from the next iteration of ExoMars because the new concept relies on a surface platform (used to deliver the Rosalind Franklin rover) that will cease functioning right after the landing. As a consequence, LaRa is now in search of another flight opportunity.

Polar motion (PM) is defined as the motion of a planet's spin axis with respect to the crust-fixed body frame (BF). The atmospheric component of the forced polar motion, resulting from mass exchanges between the polar caps and the Mars atmosphere and from atmospheric angular momentum changes, exhibits seasonal variations at annual and sub-annual periods. The external component related to external gravitational torques is precisely known as discussed in Section 2 and is therefore not considered here. Additionally, there exists a term related

* Corresponding author at: Royal Observatory of Belgium, Avenue circulaire 3, 1180 Brussels, Belgium.
E-mail address: m.goli@observatory.be (M. Goli).

https://doi.org/10.1016/j.pss.2024.105958
Received 5 May 2024; Received in revised form 15 July 2024; Accepted 29 August 2024
Available online 3 September 2024

to the well-known Chandler rotational mode (Van Hoolst et al., 2000). This free mode, called the Chandler Wobble (CW), has recently been observed by Konopliv et al. (2020) using two different approaches: (1) joint global estimates of Mars' orientation and its gravity field and (2) time series solutions of spherical harmonic coefficients C_{21} and S_{21}, from which the polar motion angles can be obtain given their relationship to the inertia matrix. While the forced polar motion amplitudes have also been estimated, their signatures in orbiter data cannot be separated from those of the seasonal changes in the gravity coefficients resulting from the redistribution of the atmospheric and ice cap mass, which is not present at the Chandler Wobble period.

Furthermore, forced polar motion is caused by two components: the matter (or mass) term, corresponding to the seasonal atmospheric mass redistribution including the polar ice cap formation, and the motion (or wind) term, corresponding to the angular momentum balance relative to the crust. The latter is expected to be non-negligible for Mars (e.g. Van Den Acker et al. (2002)). (Konopliv et al., 2020) do not distinguish between the two terms. They could be separated by utilizing a strategy involving the consistent determination of polar motion using lander data and of gravity field variations using orbiter data. By comparing the two solutions together with ice cap and atmospheric mass distribution models, it could be possible to identify the contributions of the matter and motion terms. For an in-depth discussion of the polar motion components, the reader is referred to Bizouard (2020), or Dehant et al. (2006) for the case of Mars specifically. While we do not discuss here the determination of the Chandler Wobble frequency and amplitude in great detail, a more detailed discussion can be found e.g. in Yoder and Standish (1997), Gauchez and Souchay (1999), Van Hoolst et al. (2000), Dehant et al. (2006). Given the limitations of the orbiter detection methods, an analysis of pure lander data, sensitive to both motion and matter terms but not to gravity field variations as such, is crucial to accurately determine and interpret the polar motion of Mars. Furthermore, the isolation of the matter and motion terms would provide constraints on Mars atmosphere dynamics.

In this work, we evaluate the possibility of determining the seasonal amplitudes of the polar motion of Mars using Direct-to-Earth (DTE) Doppler data from landers only, which has not been achieved up to date. This poses challenges related to the very weak signatures of polar motion in the Doppler observable at low latitudes (Le Maistre et al., 2012), and to the high correlations with the seasonal spin angle variations as discussed in this study. The determination of polar motion using a Doppler link between a lander or a rover and a polar orbiter has been considered in Yseboodt et al. (2003) and Le Maistre et al. (2018). Unlike in the case of a DTE link, the Doppler observable in this case is highly sensitive to changes in the Z coordinate of the lander. Because of that, the signature of the X and Y components of polar motion individually is longitude-dependent. However, the correlations with the spin angle will also play a role in the inability of those studies to determine both polar motion components with a single lander, in addition to the signature dependence on longitude.

The polar motion of Mars has been modelled in the past using global atmospheric circulation models. Although those models have usually focused on the influence of atmospheric and ice caps dynamics on Length-Of-Day (LOD) variations ($\Delta\phi$ in this paper) (Cazenave and Balmino, 1981; Chao and Rubincam, 1990), it has also been calculated for the polar motion. Yoder and Standish (1997) estimate the forced polar motion amplitudes, and discuss the determination of the Chandler Wobble amplitude and frequency, but their model does not include the motion term. The first attempt to model Mars polar motion amplitudes and separate the motion and mass terms can be found in Defraigne et al. (2000). The more recent model of Van Den Acker et al. (2002) uses updated climate and topography models based on data from the Mars Global Surveyor. It provides the annual and semi-annual amplitudes decomposed into motion and matter terms as shown in Fig. 1, where the motion terms are smaller than the matter terms but within the same order of magnitude. To our knowledge, no comprehensive modelling of Mars forced polar motion has been done since then.

The paper is divided in five sections. The model of Mars polar motion and its signatures in radiometric observables are described in Section 2. In Section 3, we discuss the results of analytical covariance analyses applied to different observable types, to which we turn to verify and explain some of the behaviour observed in numerical simulations presented in the following section and to evaluate the influence of lander location on polar motion determination. We then describe in Section 4 the numerical simulations results for a one-lander (Section 4.2) and two-lander scenario (Section 4.3), with the latter results used to analyse the influence of mission timing, duration and measurement noise. Then, we present the results of simulations using synthetic measurements corresponding to past missions for which radio data are available (Section 4.4), and discuss the possibility of using other kinds of radiometric data, such as range and Same-Beam Interferometry (SBI), for Mars polar motion detection with lander data (Section 4.5). We summarize our results and chart the required future work in Section 5.

2. Mars polar motion model

When transforming a vector $\vec{r}_{bf}$ from a body-fixed frame BF to a vector $\vec{r}_{if}$ in an inertial frame IF, the polar motion corresponds to the intermediary rotation from the body-fixed frame to the angular momentum frame AM:

$$\vec{r}_{if} = \mathbf{M}_{AM\to IF}\,\mathbf{M}_{BF\to AM}\,\vec{r}_{bf}, \tag{1}$$

with

$$\mathbf{M}_{BF\to AM} = R_x(Y_P)\,R_y(X_P), \tag{2}$$

where R_x and R_y are the elementary rotation matrices, and X_P and Y_P are the X and Y components of polar motion. Polar motion can be furthermore decomposed into two components: one related to the atmosphere dynamics (X_P^{Atm}, Y_P^{Atm}), and one related to the external gravitational torque (X_P^{Ext}, Y_P^{Ext}). The latter can be precisely obtained as a byproduct of the nutation theory (Baland et al., 2020a; Yseboodt et al., 2023)[1]. The external polar motion terms have different periods, and are very well known; we therefore can consider them as fixed in our simulations, which focus on the atmospheric component (comprising the matter and motion terms). The modelling and observations of the atmospheric component have been discussed in Section 1.

The atmospheric part of the polar motion components X_P^{Atm} and Y_P^{Atm} is usually written in a series with terms with frequencies corresponding to multiples of the orbital frequency of Mars, and with one term at the Chandler wobble period (e.g. Konopliv et al. 2006):

$$\begin{aligned} X_P^{Atm} &= X_{CW}^C \cos\left(n_{CW} M(t)\right) + X_{CW}^S \sin\left(n_{CW} M(t)\right) \\ &\quad + \sum_{i=1}^{4}\left(X_i^C \cos iM(t) + X_i^S \sin iM(t)\right), \end{aligned} \tag{3a}$$

$$\begin{aligned} Y_P^{Atm} &= Y_{CW}^C \cos\left(n_{CW} M(t)\right) + Y_{CW}^S \sin\left(n_{CW} M(t)\right) \\ &\quad + \sum_{i=1}^{4}\left(Y_i^C \cos iM(t) + Y_i^S \sin iM(t)\right). \end{aligned} \tag{3b}$$

where $n_{CW} = 3.3188$ is the Chandler wobble frequency in cycles per Mars year and i are the seasonal terms frequencies, also in cycles per Mars year. $M(t)$ is the Mars mean anomaly at epoch t and $(X_{CW}^C, X_{CW}^S, X_i^C, X_i^S)$ are the cosine and sine amplitudes corresponding to the Chandler wobble and seasonal frequencies of X_P^{Atm} respectively, with corresponding notation for Y_P^{Atm}. For the sake of readability, we

[1] The series for the external polar motion is available in the BMAN20.1 Mars rotation model (Baland et al., 2020b), or in Yseboodt et al. (2023), and at https://doi.org/10.24414/h5pn-7n71.

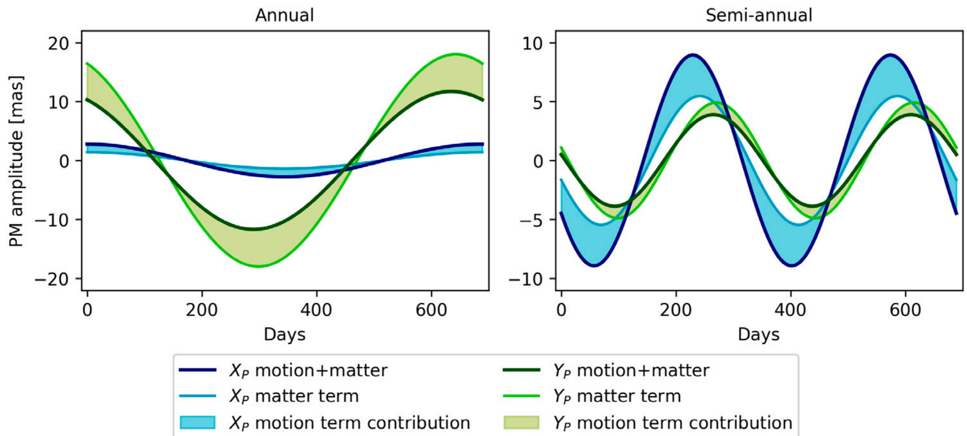

Fig. 1. The contribution of the motion (winds) and matter (atmospheric pressure and ice caps) terms to the X and Y components of the polar motion, based on Van Den Acker et al. (2002).

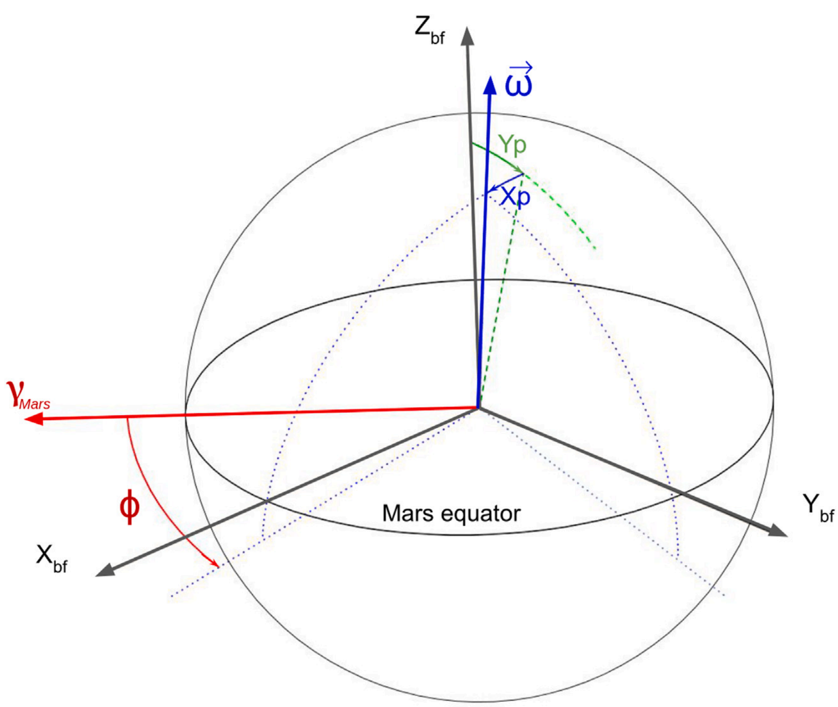

Fig. 2. The ϕ, X_p, and Y_p angles from Eq. (5). Note that in reality, the X_p and Y_p are very small, on the order of a few mas. $\vec{\omega}$ is the spin axis and γ_{Mars} is the node of the Mars true equator of date and the Mars mean orbit at J2000.

denote the atmospheric parts of the polar motion as X_P, Y_P in the rest of the paper.

Together with the polar motion, we estimate the amplitudes of the seasonal spin angle variations, defined similarly:

$$\Delta\phi = \sum_{i=1}^{4}(\phi_i^C \cos iM(t) + \phi_i^S \sin iM(t)). \tag{4}$$

This angle, along with the precession and nutation angles in obliquity (I) and longitude (ψ), is used to construct the rotation matrix $\mathbf{M}_{AM\rightarrow IF}$. The transformation between the inertial frame MMO2000 (Mars Mean Orbit at the J2000 epoch) and the BF frames can thus be written as (Folkner et al., 1997):

$$\vec{r}_{bf} = R_x(-Y_P)\, R_y(-X_P)\, R_z(\phi)\, R_x(I)\, R_z(\psi)\, \vec{r}_{\mathrm{MMO2000}}. \tag{5}$$

We show the ϕ, X_p, and Y_p angles in Fig. 2 For more discussion of the mathematical description of Mars orientation and rotation, the reader is referred to e.g. Le Maistre et al. (2012).

3. Theoretical uncertainties from the doppler and SBI observables

We investigate here the formal errors (*a posteriori* 1σ uncertainties) and correlations between three estimated parameters: the cosine amplitudes of X_P (Eq. (3a)), Y_P (Eq. (3b)), and $\Delta\phi$ (Eq. (4)) at the annual period, for one or two landers using Doppler and SBI data. To derive the equations for the covariances and the formal errors, we use first order equations in the rotation parameters for the theoretical study, building on the derivations of Yseboodt et al. (2017). The simplified analytical approach allows us to describe the underlying reasons for the results of the numerical simulations of Section 4. While we solve for all the rotation parameters together in the numerical simulations presented in the next sections, here we separate them into blocks of parameters with common temporal behaviour which therefore will be correlated, and consider only the annual cosine component as an example. This allows us to significantly simplify the analytical study.

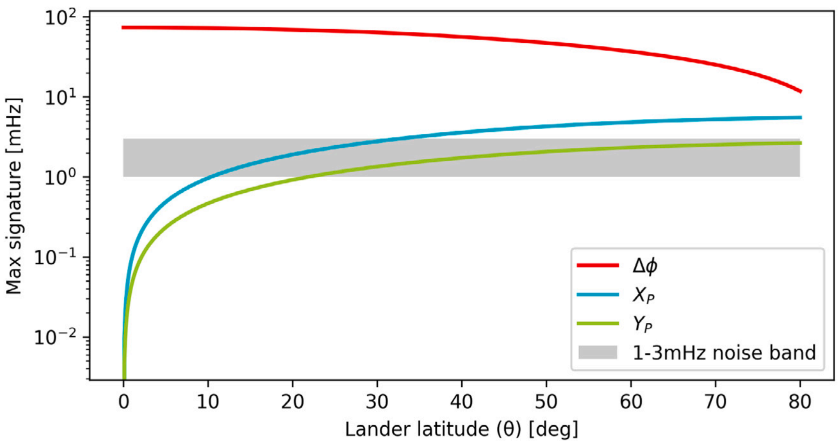

Fig. 3. The maximum theoretical signatures over 1200 days of $\Delta\phi$, X_P and Y_P in the two-way Doppler observable depending on lander latitude. We have plotted the signatures for a lander at $\lambda = 90°$, since at the first order the $\Delta\phi$ and PM maximum signatures do not depend on the lander longitude.
Source: Figure adapted from Yseboodt et al. (2017).

3.1. The derivatives of the doppler observable with respect to the rotation parameters

The partial derivatives of the Doppler observable q with respect to the rotation parameters related to the cosine of the annual frequency f_1 are:

$$\frac{\partial q}{\partial X_1^C} = -\Omega\, R\, \sin\theta\, \cos\delta_E\, \sin(H_E - \lambda)\, \cos M(t) \tag{6a}$$

$$\frac{\partial q}{\partial Y_1^C} = \Omega\, R\, \sin\theta\, \cos\delta_E\, \cos(H_E - \lambda)\, \cos M(t) \tag{6b}$$

$$\frac{\partial q}{\partial \phi_1^C} = \Omega\, R\, \cos\theta\, \cos\delta_E\, \cos H_E\, \cos M(t) \tag{6c}$$

where H_E is the Earth hour angle, δ_E is the Earth declination with respect to Mars, R is the Mars radius, Ω is the diurnal rotation rate of Mars and θ and λ are the lander latitude and longitude respectively. The derivatives with respect to the polar motion components can be rewritten to remove the lander longitude given that $H_E - \lambda = \phi - \alpha_E$, with α_E the right ascension of the Earth as seen from Mars (Yseboodt et al., 2017; Hamilton and Melbourne, 1966). Therefore, the right-hand side terms of Eqs. (6a) and (6b) are in fact independent of the longitude. One can show that the derivative of the spin angle ϕ amplitudes is in fact a linear combination of the derivatives of X_P and Y_P, with its coefficients depending on the lander position as follows:

$$\frac{\partial q}{\partial \phi_1^C} = \frac{\sin\lambda\cos\theta}{\sin\theta}\,\frac{\partial q}{\partial X_1^C} + \frac{\cos\lambda\cos\theta}{\sin\theta}\,\frac{\partial q}{\partial Y_1^C} \tag{7}$$

This linear combination is the reason why the normal matrix is singular when using Doppler data from one lander and solving for these three rotation parameters together without any additional *a priori* information. We plot the maximum signatures of the polar motion and spin angle variations in the Doppler observable in Fig. 3, adapted from Yseboodt et al. (2017).

3.2. Covariance analysis

We conduct a covariance analysis to compute the theoretical expressions for the formal errors, which will subsequently help us interpret our numerical results. To this end, we first compute the theoretical derivatives for the estimated parameters (see Section 3.1), then transform the resulting expressions to separate the different terms based on their temporal behaviour, and sum them over observation times to average out the short-period signals. We assume that over a long-term period the observation times are spaced regularly throughout the day, which results in the sums of the time-dependent terms with diurnal modulation being close to zero. We then stabilize the matrix using the *a priori* uncertainty σ_{ap} of the estimated parameters (assuming the same σ_{ap} for all three parameters). Finally, we invert the matrix and obtain the *a posteriori* covariance matrix, with the square root of its diagonal elements representing the theoretical formal errors. We describe the process in more detail in Appendix. For a more in-depth discussion of covariance analysis, the reader is referred to e.g. Montenbruck and Gill (2000).

3.2.1. Doppler observable from one lander

After applying the procedure and simplifications described above, the analytical expressions of the formal errors for X_1^C, Y_1^C and ϕ_1^C resulting from the analysis of DTE Doppler data from one lander only and adjusting the three parameters together are:

$$\sigma_{X_1^C} = \sqrt{\sigma_{ap}^2 \cos^2\theta \sin^2\lambda + \frac{2\sigma_{Dop}^2 \cos^2\theta}{\Omega^2 R^2 \sin^2\theta\, \Sigma_{Cft}}}, \tag{8a}$$

$$\sigma_{Y_1^C} = \sqrt{\sigma_{ap}^2 \cos^2\theta \cos^2\lambda + \frac{2\sigma_{Dop}^2 \cos^2\theta}{\Omega^2 R^2 \sin^2\theta\, \Sigma_{Cft}}}, \tag{8b}$$

$$\sigma_{\phi_1^C} = \sigma_{ap} |\sin\theta|, \tag{8c}$$

where σ_{Dop} is the Doppler measurement noise, σ_{ap} is the *a priori* uncertainty on the parameter in question, $\Sigma_{Cft} = \Sigma_i \cos^2\delta_E(t_i)\cos^2(f_1 t_i)$, f_1 is the annual frequency and t_i is the observation time of the ith data point. Corresponding equations apply to the other seasonal terms. Note that those expressions are not valid when the lander is exactly at the equator, as a result of the simplifications and because the polar motion signatures are null. In those cases, $\sigma_{X_1^C} = \sigma_{Y_1^C} = \sigma_{ap}$ and $\sigma_{\phi_1^C} = \sigma_{Dop}\,\sigma_{ap}\sqrt{2}\,(2\,\sigma_{Dop}^2 + \Omega^2 R^2\, \sigma_{ap}^2\, \Sigma_{Cft})^{-1/2}$.

From this, we see that as the number of Doppler observations from a single lander (and therefore Σ_{Cft}) increases, the second term in Eqs. ((8a), (8b)) decreases and the formal error of each of the three rotation parameters reaches a threshold equal to the first term, which we will refer to as a plateau in the rest of the paper, and which depends only on the lander position and σ_{ap}:

$$\sigma_{X_1^C} \approx \sigma_{ap} |\cos\theta\, \sin\lambda|, \tag{9a}$$

$$\sigma_{Y_1^C} \approx \sigma_{ap} |\cos\theta\, \cos\lambda|. \tag{9b}$$

Even if the partial derivatives of the Doppler observable with respect to X_P and Y_P are independent of the longitude (see the comment following Eqs. (6a)–(6b)), the longitude reappears in the expressions of the formal errors via the correlation with the spin angle variations

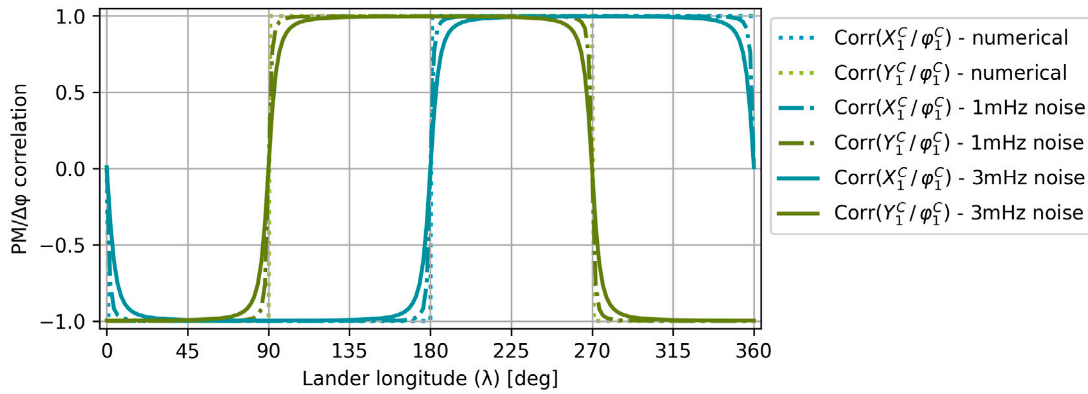

Fig. 4. Correlations between the PM and $\Delta\phi$ annual cosine amplitudes, for a single lander at latitude $\theta = 20°$. The dotted lines correspond to the simplified analytical results of Eqs. (10). The solid and dashed lines correspond to correlations computed numerically using MONTE for Doppler noise levels of 3 mHz and 1 mHz respectively for a number of observations corresponding to 2 h per week over 700 days, with a 60 s integration time (see Section 4).

amplitudes. Contrary to the formal error in the case of a single adjusted parameter, the value of the plateau for the three parameters estimated together is independent of the noise on the observable, σ_{Dop}. Eqs. (9a) and (9b) show that the formal errors of X_P and Y_P are decreasing with latitudes and are out-of-phase along the lander longitude, making it impossible to precisely estimate both X_P and Y_P at once from the tracking data of a single lander.

We note that the above expressions and conclusions are the same for the sub-annual periods, the only difference being the Σ_{Cft} value, and that Eqs. (9a) and (9b) for the plateaus are the same for range observables. We have moreover calculated the numerical values of the plateaus using Eqs. (9a) and (9b) for a set of lander longitudes and latitudes, demonstrating their good correspondence with those resulting from the numerical simulations presented in the following section.

The correlations between the rotation parameters can also be extracted from the inverse matrix. Using a few assumptions like a large number of regularly sampled data, the simplified expressions for the correlations between the cosine amplitudes are:

$$\mathrm{corr}(X_1^C, Y_1^C) = \quad \mathrm{sign}(\sin(2\lambda)) \tag{10a}$$

$$\mathrm{corr}(X_1^C, \phi_1^C) = -\mathrm{sign}(\sin(2\theta)\sin\lambda) \tag{10b}$$

$$\mathrm{corr}(Y_1^C, \phi_1^C) = -\mathrm{sign}(\sin(2\theta)\cos\lambda) \tag{10c}$$

These equations are consistent with the numerical results discussed in Section 4. We show in Fig. 4 the correlations between X_1^C, Y_1^C and ϕ_1^C terms resulting from the analysis of Doppler data acquired from a single lander located at 20°N latitude and at a longitude varying between 0° and 360°. Both numerical and analytical correlations are shown in this figure. Note that the correlations follow a similar pattern for the sine terms, as well as for the other seasonal terms.

In the upcoming sections we demonstrate that the correlations between the spin angle variations and the seasonal polar motion components make it impossible to determine the latter using a single lander. This provides a possible explanation for the failure to observe polar motion in the Viking-1 and InSight/RISE data analysis of Le Maistre et al. (2023). This study yielded precise estimates of the other main Mars rotation and Orientation Parameters (MOP), including the spin angle variations series and Free-Core-Nutation (FCN) parameters, but did not determine polar motion that was fixed to the value of Konopliv et al. (2020). We think this is primarily due to the fact that a different set of rotation angle variation amplitudes was estimated by these authors for each mission separately (because of the incompatibility of the two datasets in this regard), which is equivalent to using two single landers separately from the point of view of polar motion estimation. Furthermore, the uncertainty in the ephemeris and other rotation parameters over long time periods will also significantly increase the polar motion formal errors, as discussed in Section 4.3.3.

3.2.2. Doppler observable from two landers

We repeat the above steps for the case where data from two landers are used. The results obtained using the analytical expressions are consistent with those obtained using a full numerical simulation (Section 4). While the resulting analytical expressions for the formal errors (σ_{post}) are quite lengthy and will not be recounted here, we use them to evaluate the influence of various combinations of lander locations on the polar motion solution, and describe their derivation in Appendix. We use the timing of 2 h per week, with a measurement every 60 s, over 700 days.

We investigate the effects of the absolute and relative positions of the two landers, separating the effect of latitude and longitude. In Fig. 5, we plot the formal errors as a fraction of the *a priori* uncertainty for a range of lander latitudes, fixing their longitudes at the same value of 15°. In Fig. 6 we repeat this for a range of lander longitudes with their latitudes fixed at 20°. In both figures, we have marked the locations corresponding to the scenario assumed for the other figure.

Predictably, we observe that when both landers are close to the equator, neither component of the polar motion can be determined due to the weak signatures at those latitudes. When the landers are close in latitude but further away from the equator, the ability to determine both the X and Y polar motion components depends on the ability to decorrelate the polar motion and spin angle terms, and therefore on the landers' longitudes. The smaller the value of $|\cos(\lambda_2 - \lambda_1)|$, the smaller the dependence of the solution on the separation in latitude outside of the $\theta_1 = \theta_2 = 0°$ region. As the longitudinal separation modulo 180° decreases and $|\cos(\lambda_2 - \lambda_1)|$ increases, the ability to determine the polar motion components again becomes dependent on latitude, with the determination becoming impossible at $\theta_1 = \theta_2$ for $\cos(\lambda_2 - \lambda_1) > 0$ and $\theta_1 = -\theta_2$ for $\cos(\lambda_2 - \lambda_1) < 0$. The latter case corresponds to the slopes of the "bad" regions where the formal error is driven by the *a priori* uncertainty in Fig. 5 being reversed.

This is further illustrated in Fig. 6. The diagonals in Figs. 5 and 6 represent a situation in which the two landers occupy the same location, and therefore are representative of the results obtained with a single lander in that position as discussed in the previous subsection[2]. For off-diagonal scenarios, when the two landers are not close to each other in longitude, we see that the addition of the second lander results in an improvement even when both landers are each at a longitude that would individually make a single-lander estimation impossible (90° and 270° for X_P, and 180° and 360° for Y_P). This is due to the decorrelation between the X_P/Y_P and $\Delta\phi$ terms, as shown in Fig. 4.

[2] Increasing the number of observations by N results in an approximately $\sqrt{N}$ improvement in formal errors in the "good" regions, but their ratio becomes equal to 1 in the "bad" regions where the formal errors are strongly driven by the *a priori*.

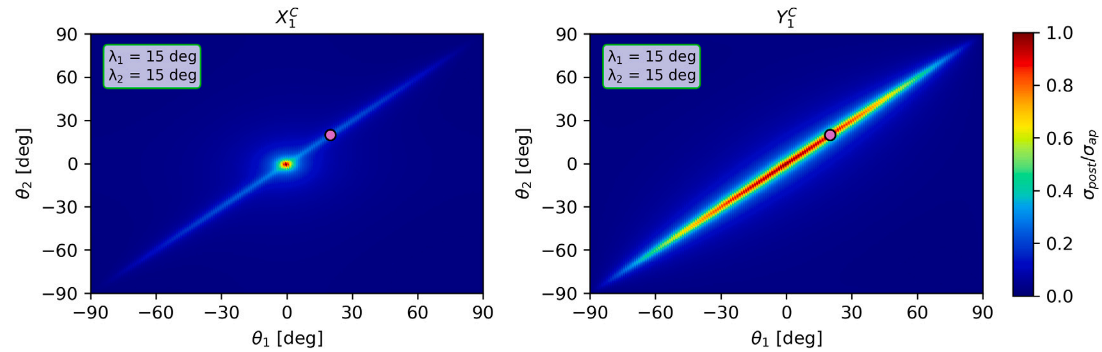

Fig. 5. The formal errors of the annual cosine X (left) and Y (right) terms of polar motion using Doppler data from two landers, as a fraction of their *a priori* uncertainty, as a function of their latitudes. The longitudes of the two landers have been fixed at 15°. The purple circles correspond to the scenario plotted in Fig. 6 where $\theta_1 = \theta_2 = 20°$.

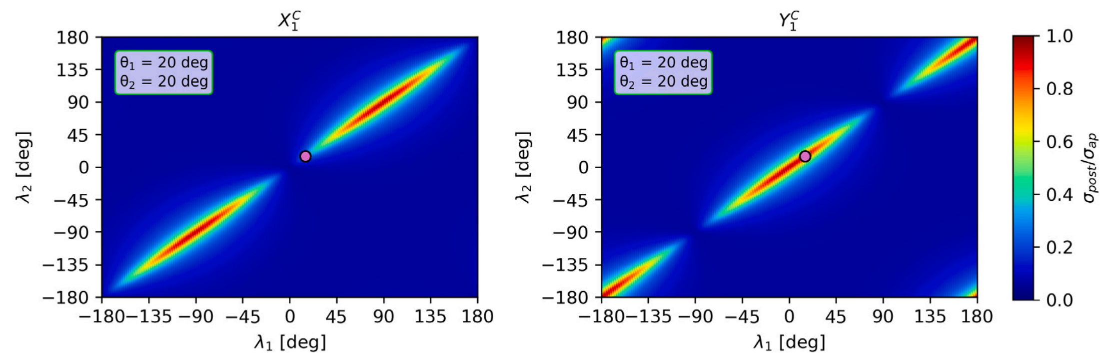

Fig. 6. Formal errors on the annual cosine term of polar motion for two landers at a latitude of 20°, as a fraction of their *a priori* uncertainty, as a function of their longitudes. The purple circles correspond to a scenario plotted in Fig. 5 where $\lambda_1 = \lambda_2 = 15°$.

Note that Figs. 5 and 6 were generated by calculating the two-lander formal errors for an *a priori* uncertainty value of 30 mas on all terms, and with the Doppler noise of 3 mHz ($\approx$ 0.05 mm/s). The noise of the observations influences the extent of the regions where the formal errors are driven by the value of the *a priori* uncertainty; the lower the noise, the more limited their extent. This is consistent with the correlations between the polar motion and spin angle terms plotted in Fig. 4. We discuss this in more detail in Section 4.3.4.

3.2.3. Same-beam interferometry observables

We repeat the above steps for the Same-Beam Interferometry (SBI) case, which, by definition, requires the simultaneous tracking of two or more landers. The SBI observable is the differential phase of the carrier signals of the two landers tracked from the same ground station, from which the differential range between the two landers can be obtained (Folkner and Border, 1990; Border et al., 1991; Gregnanin, 2014). We consider SBI measurements alone in this section, however in practice they could be combined with the carrier (i.e. Doppler) measurements from one of the landers. This is discussed further in Section 4.5. We model the SBI observable directly as the differential range between the two landers, and adopt the conservative X-band noise value of 10 mm (Gregnanin, 2014). We use the timing of 2 h per week, with a measurement every 300 s.

Following (Yseboodt et al., 2017), the partial derivatives of the annual cosine amplitude of the polar motion and spin angle components in the range observable ρ are:

$$\frac{\partial \rho}{\partial X_1^C} = R\left(-\sin\delta_E\cos\theta\cos\lambda + \cos\delta_E\sin\theta\cos\left(\lambda - H_E\right)\right)\cos M(t) \quad (11a)$$

$$\frac{\partial \rho}{\partial Y_1^C} = R\left(\sin\delta_E\cos\theta\sin\lambda - \cos\delta_E\sin\theta\sin\left(\lambda - H_E\right)\right)\cos M(t) \quad (11b)$$

$$\frac{\partial \rho}{\partial \phi_1^C} = R\cos\theta\sin H_E\cos\delta_E\cos M(t) \quad (11c)$$

The partial derivatives of a differential range observable with respect to the rotation parameters are the difference between the partial derivatives of the range observable for each lander, of which the Doppler observable partials (Eqs. (6a)–(6c)) are the time derivatives.

We follow the same procedure as that outlined for the Doppler case to obtain the equations for the formal errors as a function of the landers' locations. The resulting equations are quite long and will not be recounted here. However, when plotted for a range of baseline orientations and midpoint coordinates in Fig. 7, we find again that the optimal locations for X_P, Y_P and $\Delta\phi$ determination with SBI are mutually exclusive regardless of the baseline location and orientation. In most cases we will be entirely unable to determine at least one of those. An increase in the baseline length does not significantly alleviate the problem, as (for most baselines) it will again improve the determination of some of the parameters while increasing the formal errors for the remaining ones. In the SBI case, this is due to two factors. First, as in the Doppler case, the polar motion and spin angle terms are highly correlated, and their decorrelation requires the use of more baselines or the combination of the SBI observable with e.g. the Doppler observable from one of the landers. We discuss this in more detail in Section 4.5. Furthermore, the signature of X_P and Y_P in the range (and therefore differential range) observable contains a term that is dependent on the lander's longitude. This reflects the range observable's sensitivity to changes in the Z coordinate of the lander, which is not the case for the Doppler observable (Yseboodt et al., 2017; Le Maistre, 2016). For baselines aligned with the parallel, as is the case for the bottom row of Fig. 7, this effect becomes dominant.

The results shown in Fig. 7 reflect a combination of those two effects. In both cases, the resulting formal errors of the polar motion components are still driven by the *a priori* uncertainty. The use of three landers in optimal relative locations, and therefore of three baselines, could alleviate this issue. This would also eliminate the bad regions in the Doppler-only scenario described in previous subsection. However,

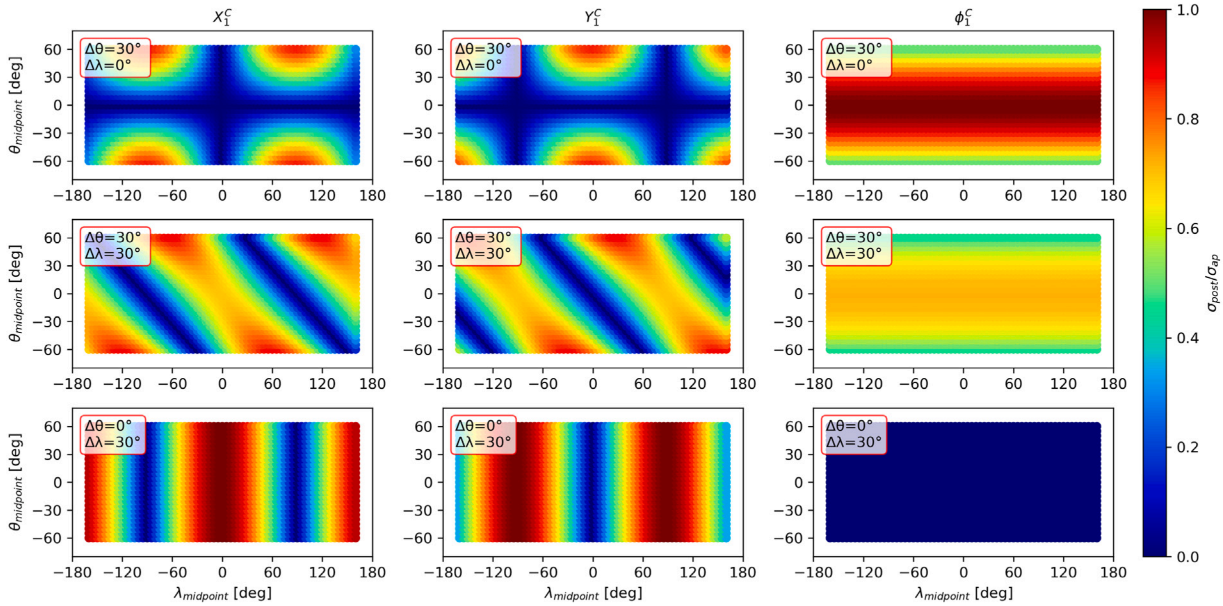

Fig. 7. The theoretical formal errors for the annual cosine X_P, Y_P and $\Delta\phi$ terms estimated from SBI measurements, as a fraction of the *a priori* uncertainty and depending on the baseline midpoint and the latitudinal and longitudinal separation of the two landers ($\Delta\theta$ and $\Delta\lambda$ respectively). In the case of ϕ_1^C, when the baseline is aligned with the parallel (i.e. $\Delta\theta = 0°$), ϕ_1^C is very well determined and the formal errors do not depend on the baseline location. This behaviour is also illustrated in the last row of Fig. 15.

in this work we focus on scenarios with only two landers, which are considered more likely to occur in the near future. In Section 4.5, we compare the performance of SBI to that of Doppler only, range only, and SBI combined with Doppler.

4. Numerical simulations

4.1. Simulation details

In this section, we present and compare the results of numerical simulations involving Doppler tracking of a single lander versus two landers in terms of their ability to determine Mars polar motion and spin angle variation amplitudes. We discuss the influence of mission operational parameters other that the landers' locations, in particular mission duration and timing and the noise level. We also compare the results obtained using Doppler observables with range and SBI ones.

The Jet Propulsion Laboratory's MONTE-Python library (Evans et al., 2018) is used to generate the synthetic measurements and estimate the parameters of interest using an iterative least-squares procedure. We simulate two-way Doppler measurements from hypothetical landers in order to understand the influence of various mission parameters on the determination of polar motion from landers, and the improvement enabled by using multiple landers' data. We use numerical simulations due to the limitations of the simplified method in the preceding sections, allowing us to accurately consider the case in which all terms are estimated, as well as the additional effect of bias and uncertainty associated with other parameters.

Unless specified otherwise, in all scenarios we are assuming two tracking windows of 1 h each per week, carried out over a full range of line-of-sight elevation angles (i.e. from grazing angles near zero elevation up to Earth maximum elevation at the time of the year). The values of the Mars orientation and rotation parameters used are listed in Table 1. In Section 4.3.3, we show the results of the simulations in cases with a larger set of estimated parameters (the fixed terms in Table 1 and lander positions), which are kept fixed in the rest of this section as we have found that including them does not alter the conclusions regarding polar motion determination. We assume measurements in X-band with a conservative measurement noise of 3 mHz (≈ 0.05 mm/s) at 60 s integration time. This value is taken based on the expected noise level of LaRa measurements on Mars and comprises instrumental and propagation noise and systematic errors (Dehant et al., 2020). Certain modern instruments, such as the RISE instrument on the InSight mission, can achieve values that are 2–3 times lower after calibration (Buccino et al., 2022; Le Maistre et al., 2023)). To ease the discussion, in certain cases we plot and discuss the cumulative uncertainties of X_P, Y_P and $\Delta\phi$ on all the amplitudes/frequencies derived using the standard equations for the variance of sums and products, rather than those of the individual sine and cosine per-term amplitudes. Therefore for X_P, the quantity computed and plotted is σ_{X_P}:

$$\begin{aligned}\sigma^2_{X_P} &= \sum_i \left[\mathrm{Var}(X_i^S)\cdot(\sin\omega_i t)^2 + \mathrm{Var}(X_i^C)\cdot(\cos\omega_i t)^2\right] \\ &+ 2\sum_{i<j}\left[\mathrm{Cov}(X_i^S, X_j^S)\cdot\sin\omega_i t\sin\omega_j t + \mathrm{Cov}(X_i^C, X_j^C)\cdot\cos\omega_i t\cos\omega_j t\right] \\ &+ 2\sum_{i\leq j}\left[\mathrm{Cov}(X_i^S, X_j^C)\cdot\sin\omega_i t\cos\omega_j t + \mathrm{Cov}(X_i^C, X_j^S)\cdot\cos\omega_i t\sin\omega_j t\right]\end{aligned} \tag{12}$$

with $i,j = 1,\ldots,4$ corresponding to the seasonal terms and $i,j = 5$ to the Chandler wobble term (see Eq. (3)), for t corresponding to the maximum value of σ_{X_P} over the observation period. Corresponding equations are used for Y_P and for $\Delta\phi$ (with the exception of the Chandler term for the latter).

4.2. Single lander case

Here we jointly estimate the polar motion and spin angle variations amplitudes (see Table 1) using simulated data from a single lander. We plot the results for the annual cosine components in Fig. 8, the other seasonal terms following a similar pattern. Our numerical results correspond to the expected formal errors of Section 3.2. The opposite dependence of the X_P and Y_P components of polar motion on longitude can be again clearly observed in both panels of Fig. 8, showing the impossibility of obtaining a good estimate of both X_P and Y_P from a single lander as predicted by Eqs. (9a) and (9b). In particular, the behaviour of the X_1^C and Y_1^C formal errors in the bottom panel is the same as that in Fig. 6 when $\lambda_1 = \lambda_2$.

We also note that the formal errors shown in this figure behave in a way that is consistent with the theoretical maximum signatures of

Table 1
Mars rotation model values used in the simulations. Sources: (1) Le Maistre et al. (2023), (2) Konopliv et al. (2020) We have used larger *a priori* uncertainties than those found in (1) and (2) to understand their effect on PM determination, as discussed in Section 3.

Parameter	Symbol	Value	A priori	Source
Obliquity at J2000	I_0	25.189409°	Fixed	(1)
Obliquity rate	$\dot{I}$	−7.99 mas/year	Fixed	(1)
Spin angle at J2000	ϕ_0	133.386394°	Fixed	(1)
Spin rate	$\dot{\phi}$	350.89198534°/day	Fixed	(1)
Node longitude at J2000	ψ_0	81.968359°	Fixed	(1)
Precession rate	$\dot{\psi}$	−7598.1 mas/year	Fixed	(1)
Core factor	F	0.0615	Fixed	(1)
FCN period	τ_{FCN}	−243 day	Fixed	(1)
Spin angle variations				
Annual amplitudes	ϕ_1^S, ϕ_1^C	−176.5 mas, 400 mas	30 mas	(1)
Semi-annual amplitudes	ϕ_2^S, ϕ_2^C	−134.4 mas, −109.1 mas	30 mas	(1)
Ter-annual amplitudes	ϕ_3^S, ϕ_3^C	−22.2 mas, −9.7 mas	30 mas	(1)
Quarter-annual amplitudes	ϕ_4^S, ϕ_4^C	−11.7 mas, 0.4 mas	30 mas	(1)
Polar motion				
Annual amplitudes	X_1^S, X_1^C, Y_1^S, Y_1^C	23.3, −17.6, −0.6, −8.6	30 mas	(2)
Semi-annual amplitudes	X_2^S, X_2^C, Y_2^S, Y_2^C	3.4, −10.9, −0.4, −1.9	30 mas	(2)
Ter-annual amplitudes	X_3^S, X_3^C, Y_3^S, Y_3^C	0.9, −0.6, −2, −6.8	30 mas	(2)
Quarter-annual amplitudes	X_4^S, X_4^C, Y_4^S, Y_4^C	1.7, −7.3, 1.3, −3.8	30 mas	(2)
Chandler Wobble amplitudes	X_{CW}^S, X_{CW}^C, Y_{CW}^S, Y_{CW}^C	6.5, −1.7, 1.2, 5.1	30 mas	(2)

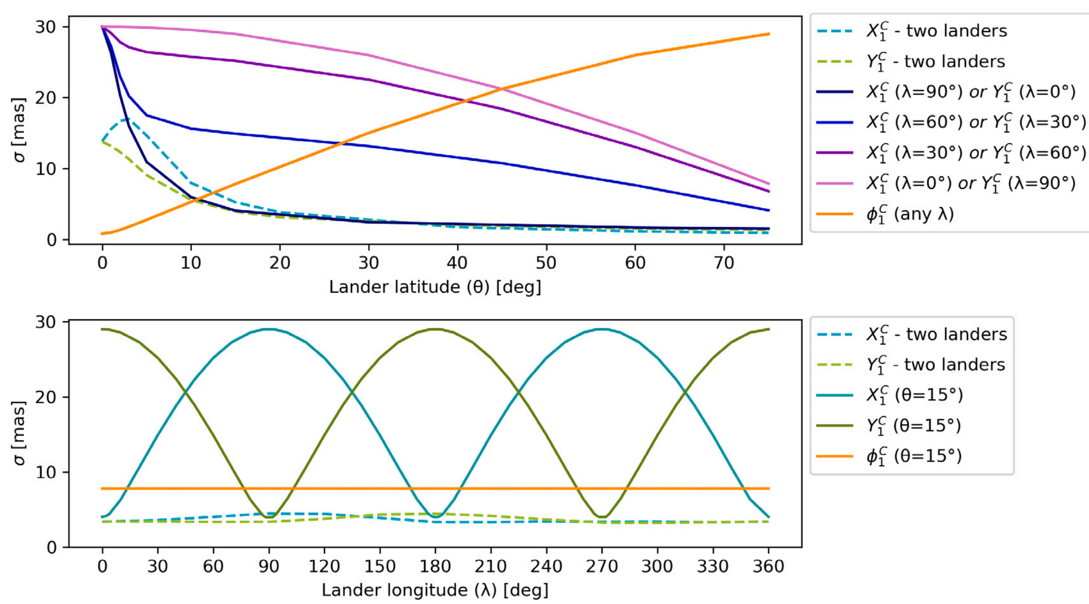

Fig. 8. Comparison of the X_P, Y_P and $\Delta\phi$ formal errors after approximately one Martian year of observations. We plot the annual cosine components as the other seasonal terms show a similar behaviour. The solid lines correspond to simulations using data from a single lander, while the dashed lines show the uncertainties for a two-lander scenario. The top panel shows the solution uncertainty for a single lander at four different longitudes over a range of latitudes. In the bottom panel, the lander latitude is fixed at 15° and its longitude is varied between 0° and 360°. In the two-lander cases, we place the landers at the InSight and MSR/Perseverance locations, (4°, 136°) and (18°, 78°) respectively. We fix the position of the first lander, and vary the latitude of the second lander in the top panel and its longitude in the bottom panel.

each parameter, which are, to the first order, equal to their partials in Section 3.1 times the parameter value. Indeed, close to the equator we observe the increase of polar motion uncertainties and decrease of $\Delta\phi$ uncertainties, the inverse being the case for their respective maximum signatures as shown in Fig. 3.

4.3. Two landers case

We have established in Section 3 the necessity of using data from more than one lander to determine the X_P and Y_P amplitudes. This is illustrated in Fig. 8 where a solution obtained using two landers is plotted together with that obtained with a single lander. For the former, the lander locations correspond approximately to the InSight and Mars Sample Return (MSR, same location as Perseverance) locations, with varying latitude and longitude of the second lander. Note that the increase in X_P formal error for two landers in the top panel around $\theta = 4°$ corresponds to an unfavourable situation where the latitude of the two landers is the same. We focus in this subsection on reviewing the mission parameters that can contribute to this improvement in addition to the respective locations of the landers, such as mission scheduling and timing and the observable noise. This is relevant as most of the available radiometric data comes from landers operating at different epochs and for different mission durations.

4.3.1. Mission duration and lander baseline

We first plot the resulting X_P, Y_P and $\Delta\phi$ formal errors for selected baselines in Fig. 9, for cases where we combine the data from two landers as well as for each lander separately. The baselines were selected to act as representative scenarios. We have simulated the missions for up to 1400 Earth days to demonstrate that in the two lander case, the solution stabilizes shortly after 1 Martian year to a value consistent with the analytical results of Section 3.2.2. We again observe that for single lander data, the formal errors are in most cases highly dependent on the *a priori* uncertainties. For confirmation, we repeated those selected simulations with *a priori* uncertainties up to 100 mas and 4 Martian years, and observed the solution plateauing at a level that depends on the *a priori* value according to Eq. (9) after 1–3 Martian years depending on the lander latitude (and therefore the strength of the polar motion signature). This behaviour disappears once we consider data from two landers, and solutions with different *a priori* uncertainties converge to similar *a posteriori* ones following the decorrelation of the various seasonal terms from each other. It is clear that the improvement is due to the relative positioning of the landers and not due to the increased amount of data, in which case we would expect an improvement of approximately $\sqrt{2}$. This benefit is evident in cases where the results from each lander are individually equally poor, as is the case e.g. for X_P in row 2 of Fig. 9. Conversely, we observe that when both landers are very close to the equator (two bottom rows) the polar motion solution remains poor and takes far longer to stabilize, corresponding to the red region around $\theta_1 = \theta_2 = 0°$ in Fig. 5. While the longitudinal separation of the landers still allows us to decorrelate the polar motion terms from the spin angle ones (this can be seen by the improvement in the X_P determination), the formal errors remain high; this is due to the very weak signature of the polar motion at those latitudes. The increase in longitudinal separation of the landers does not significantly alleviate the issue; however, the problem disappears once at least one of the landers is placed at a higher latitude, as seen in rows 1, 2 and 4.

4.3.2. Duration of the second mission

We look at the influence of the duration of the second lander's mission, with the duration of the first lander's mission fixed at 700 days and the duration of the second mission within the 70–700 days range, and with the two missions starting at the same time. In this and the next subsections, we fix the lander positions at $\theta_1 = 2°, \lambda_1 = 30°$ and $\theta_2 = 30°, \lambda_2 = 150°$, selected as one of the representative optimal baselines in row 1 in Fig. 9. The results are shown in Fig. 10. While we find that with such an optimal baseline, 10 weeks of data from the second lander already results in formal error improvement between approximately 10% and 25% depending on the term with respect to the single lander solution, data from a full Martian year is required to fully benefit from the two lander advantage. Fig. 10 also illustrates the clustering of polar motion terms in two distinct groups, represented by the blue and red lines in the plot. The blue lines correspond to frequencies that are harmonics of the quarter-annual frequency; the red lines correspond to the ter-annual and Chandler Wobble terms whose frequencies are close to each other (229 and 207 days respectively), which explains the longer time needed for decorrelation.

4.3.3. Total time coverage and the effect of mismodelling

We consider the possibility of combining data from missions operating at two different epochs, each over 700 days. Assuming that the adopted rotation models are consistent between the two time periods and that there are no additional error sources that accumulate with time such as ephemeris error, we predictably find that there is no discernible change in the solution depending on the total time coverage, with the periodic variations in the solution resulting from the periodic changes in the observation geometry. Those variations can be observed in the results plotted in Fig. 11.

We note, however, that this is a fairly optimistic assumption. In reality, the model used will have to correctly account for the changes in the rotation and orientation of Mars over longer time periods. This has proven challenging so far when combining data from landers operating at widely separated time periods, e.g. in the case of the $\Delta\phi$ terms estimation in Le Maistre et al. (2023). Furthermore, the effect of ephemeris error over time might also influence the ability to determine the polar motion.

To evaluate the effect of those, we have simulated a number of cases for a pair of landers with the same baseline and observation timing as in the previous subsections accounting for the mismodelling and uncertainty of lander positions and other orientation parameters. The additional parameters and their uncertainties and biases are listed in Table 2. We have also accounted for ephemeris mismodelling by adding a bias corresponding to the difference between the DE440 (Park et al., 2021) and INPOP21 (Fienga et al., 2021) ephemerides without fitting the ephemeris.

In Fig. 12, we plot the solution for the annual cosine amplitude. The conclusions are similar for other seasonal terms. We compare the results for missions operating at the same time (starting in 2018), and at different times (starting in 1976 and 2018, corresponding to Viking 1 and InSight i.e. the longest time span for which there is radio data available). In both scenarios, we observe an initial influence of the lander position uncertainty (case 2 in the figure legend), however after a full Martian year of observations the resulting polar motion and $\Delta\phi$ uncertainties become independent of it. We have assumed an initial position uncertainty of 10 m, which is attainable by combining tracking data with a topography model (Le Maistre, 2016). The solution starts to degrade for position uncertainties above approximately 50 m. In the case of two missions operating at the same time (top row of Fig. 12), the uncertainties in the other rotation parameters and the ephemeris do not significantly influence the solution (cases 3–5, with all the curves overlapping in the plot). In the case of two missions operating at different times (bottom row), we predictably observe an effect of uncertainties of the time-varying rotation parameters (case 4). Furthermore, ephemeris mismodelling directly affects the formal errors of the spin angle (case 3), as well as those polar motion indirectly by increasing the formal errors of the other estimated rotation parameters (case 5). We plot here the worst-case scenario, with the effect decreasing the closer in time the two missions are to each other. Those challenges will have to be addressed by future analyses of data from older missions.

4.3.4. Measurement noise

We now briefly discuss the influence of the noise of the Doppler observable on the formal errors. When the resulting formal errors are independent of the *a priori* uncertainty value, they are proportional to the Doppler noise. However, we also find that lowering the noise results in the narrowing of the "bad" regions where the formal error is driven by the *a priori* uncertainty. This is consistent with the correlations between the polar motion and spin angle variation terms as shown in Fig. 4. In Fig. 13, we plot the formal errors of the annual cosine X component of polar motion for different values of the Doppler noise and *a priori* uncertainties, with the other simulation settings being the same as in the previous subsections. The formal errors are independent of the *a priori* when their results overlap; in contrast, the closer the longitude of the second lander λ_2 is to $\lambda_1 = 90°$ the more it is driven by the *a priori*. We note that the region where the formal errors are driven by the *a priori* is narrower in the 1 mHz case than in the 3 mHz case ($\sim 75°$ to 90° and $\sim 50°$ to 90° respectively, in the case where their latitudes are $\theta_1 = \theta_2 = 20°$).

4.4. Synthetic data from real landers

We briefly extend our considerations to the possibility of estimating polar motion using available data from past missions. We generate synthetic measurements using real data timestamps and noise levels, and evaluate the improvement enabled by the combination of multiple landers. We use noise values of 1.4 mHz (0.02 mm/s) for InSight X-band and 5.3 mHz (0.09 mm/s) for Viking-1 S-band. The results are shown in Fig. 14 for each polar motion term. We find that the combination of InSight and Viking-1 data alone improves the InSight solution by over

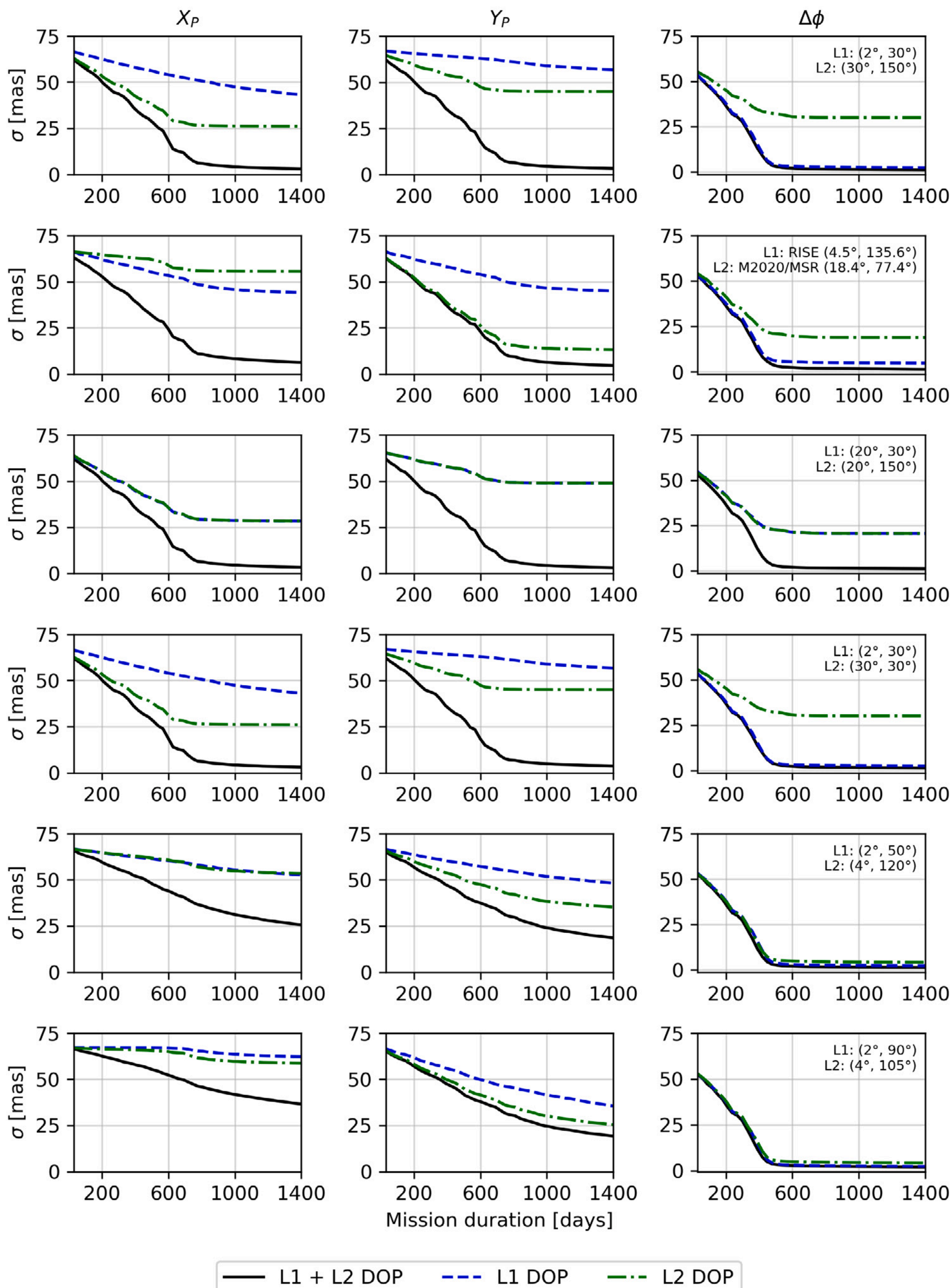

Fig. 9. Evolution of the cumulative formal errors for X_P, Y_P and $\Delta\phi$ terms over mission durations of up 1400 days (2 Martian years), using Doppler data from two landers (L1 and L2) at selected location baselines, which have been chosen as representative from a larger simulation set.

100%, bringing the sigmas below 10 mas. The addition of the other landers only improves the solutions by a few more mas.

We note, however, that polar motion determination data from past missions is challenging as discussed in Section 4.3.3, and is the subject of ongoing work. In particular, we will reevaluate the approach of Le Maistre et al. (2023) and the possibility of estimating polar motion along with a single spin angle series from combined Viking-1 and InSight data, as mentioned in Section 3.2. If the LaRa instrument succeeds in finding a flight opportunity to Mars, its data will also be combined with the aforementioned two spacecraft, resulting in further improvement to the polar motion model together with the other rotation and orientation parameters.

4.5. Discussion about other techniques

We repeat the simulations for two landers at selected locations using other types of observables: range, SBI, and SBI combined with Doppler. We assume conservative noise values of 10 mm for the X-band SBI measurement (Gregnanin, 2014) and 1 m for the range measurement (Folkner et al., 1997).[3] We model the SBI observable as the differential range between the two landers. The results, again over one Martian year of observations, are plotted in Fig. 15. Consistent

[3] We have also repeated the simulations for achievable 1 mm (in Ka-band) and 30 cm noise values respectively, with the conclusions remaining the same.

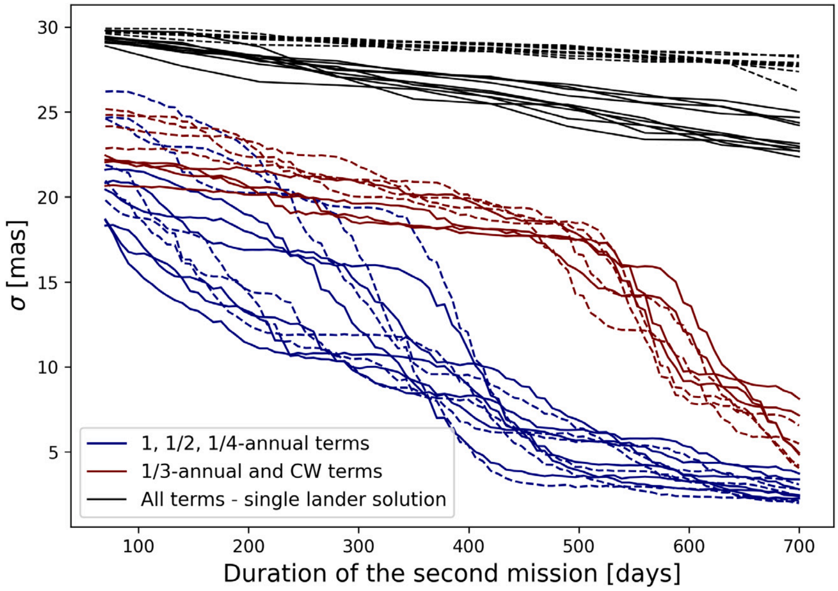

Fig. 10. Influence of the duration of the second mission on the improvement in PM parameters determination resulting from including data from two landers, with the first mission operating for around 1 Martian year. The solid and dashed lines represent the X_P and Y_P amplitude terms respectively.

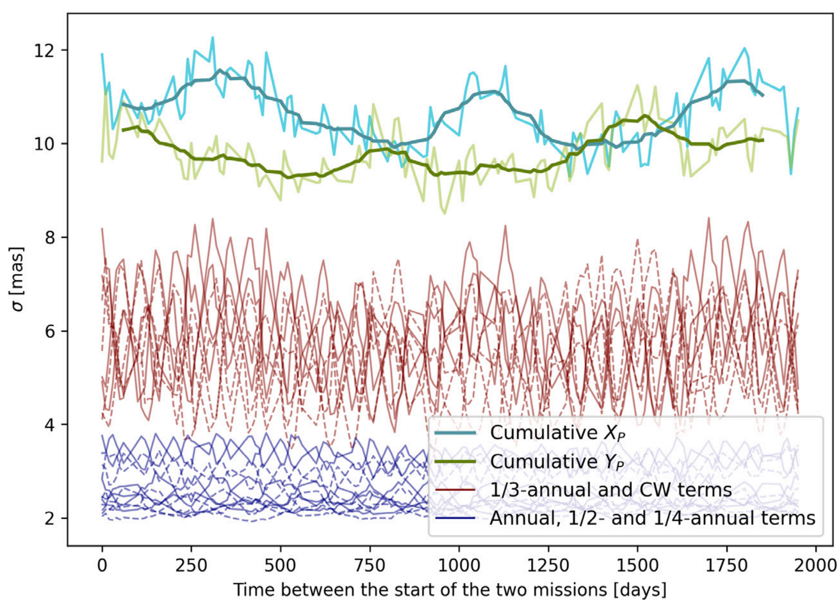

Fig. 11. Influence of the difference in the missions' starting time on the improvement in PM determination resulting from including data from two landers, with the first mission beginning in June 2021 and both missions operating for approximately one Martian year (700 days). The thin blue and red lines represent the 1σ solution uncertainties of the individual PM terms, and the blue and green lines represent the cumulative values for the X_P and Y_P components respectively. A moving average is plotted over the simulation results for the cumulative values.

with the theoretical derivations in Section 3 and the resulting formal errors in Section 3.2.3, we note that it is not possible to estimate both components of the polar motion together with spin angle variations using SBI alone. However, the SBI observable is actually the differential phase of the carrier signals of the two spacecraft (Folkner and Border, 1990; Border et al., 1991), therefore we also have access to the individual landers' Doppler data and can combine the two. Combining SBI with Doppler data from one of the landers (using Doppler data from both landers plus SBI would result in the same data being used twice, by construction of the SBI observables), we obtain results comparable to or better than those using Doppler or range alone, depending on the baseline location. Furthermore, when using SBI, the formal errors stabilize after less than a complete Martian year for baselines which are not sensitive to the spin angle variations, i.e. ones not aligned with the parallels (rows 1 to 3 in Fig. 15). The addition of Doppler data sensitive to $\Delta\phi$ mitigates this. This indicates that SBI might also be an attractive technique for missions with durations shorter than the Martian year, unlike with traditional Doppler data as discussed in Section 4.3.2. For the baselines not aligned with the parallel and where the two-lander Doppler solution is already sensitive to polar motion (rows 2 and 3 in Fig. 15), combining Doppler and SBI results in formal errors of the polar motion that are also significantly lower than the SBI-only ones, even when SBI alone is capable of estimating a given parameter. Finally, in row 4, the baseline is aligned with the parallel. In this case, the signature of X_P and Y_P in the SBI observable is entirely dependent on the landers' longitudes, as discussed in Section 3.2.3. The combination of SBI and Doppler data again mitigates this and results in significantly lower formal errors than the Doppler solution.

Table 2
The parameters added to the estimation with their uncertainty and the bias. For the symbols and the nominal values of the parameters, and the uncertainties associated with the $\Delta\phi$ and PM terms, the reader is referred to Table 1. The rotation and orientation parameters *a priori* uncertainties correspond to 3σ of the (Le Maistre et al., 2023) solution.

Parameter	1σ uncertainty	Bias
Mars rotation and orientation parameters:		
Obliquity at J2000	0.0000192 deg	–
Obliquity rate	3.9 mas/year	1.3 mas/year
Spin angle at J2000	0.0000222 deg	–
Spin rate	0.000000033 deg/day	0.000000011 deg/day
Node longitude at J2000	0.000039 deg	–
Precession rate	6.6 mas/year	2.2 mas/year
Core factor	0.021	0.007
FCN period	0.06 deg/day	0.02 deg/day
CW frequency	0.0126 deg/day	0.0042 deg/day
Lander x, y, z coordinates	10 m	10 m

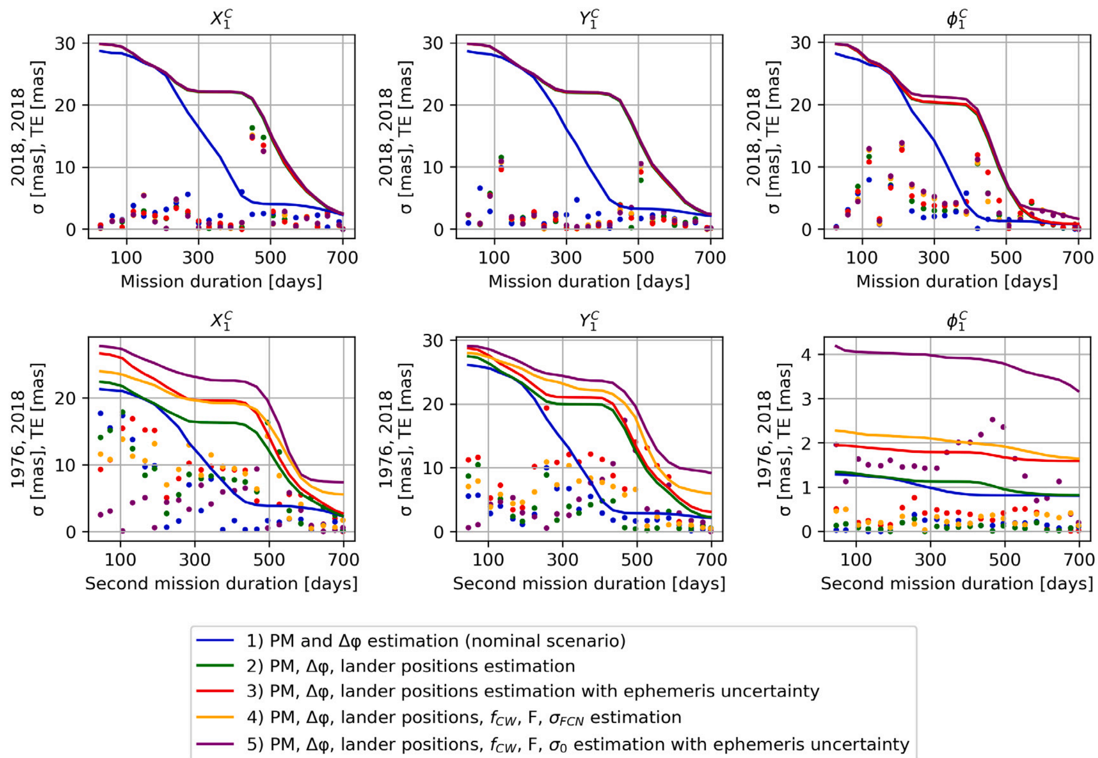

Fig. 12. The influence of uncertainty and mismodelling of lander coordinates, other rotation parameters, and the ephemeris on polar motion and spin angle variations determination. The solid lines correspond to formal errors (σ) and the circles to true errors (TE). In the top row, cases 2–5 overlap.

This demonstrates the complementarity of SBI with the traditional techniques of Doppler and range and its utility in improving on their capabilities. In a future study, we will evaluate the optimal SBI baselines and mission architecture requirements in more detail. We note, however, that a combined two-lander SBI plus one-lander Doppler estimation is sufficient to estimate all three parameter groups for all of the diverse baselines in Fig. 15, indicating that it does not suffer from the "bad" region limitation (where the formal error is driven by the *a priori* uncertainty, as discussed in Section 3.2.2) of a two-lander Doppler-only estimation. We observe a very similar behaviour of the combined range data from two landers to that of combined Doppler data. This is due to the fact that the behaviour of the formal errors is primarily driven by the correlations between the polar motion and the spin angle and the geometrical information in the observables. Similarly, combining SBI and range data results in very similar behaviour to that of combined SBI and Doppler data, as it is the combination of any line-of-sight information with SBI that provides plane-of-sky constraints and enables the simultaneous determination of polar motion and the spin angle variations.

We note, however, that SBI is not a technique that has been extensively implemented in practice. It requires the simultaneous operation of identical coherent transponders; to fully benefit from its advantages, they should be operating at the same frequency, with the signals distinguished by their CDMA (Code Division Multiple Access) codes (Gregnanin, 2014). This is challenging, given the high cost and therefore limited number of Mars missions in any given launch window. Furthermore, at the level of precision offered by SBI, the modelling of the differential phase delays of the transponders due to uncorrelated effects and a closer evaluation of the achievable overall error budget become crucial.

It is worth mentioning that a preliminary study involving combined SBI and Doppler in a three-spacecraft baseline configuration was performed by Gregnanin (2014), showing that such a scenario offers a better opportunity to further constrain Mars rotation and interior models. In fact, it could also eliminate the problem of the bad regions in the Doppler-only scenarios. Nevertheless, a mission relying on three simultaneously-operating landers is challenging and considered less

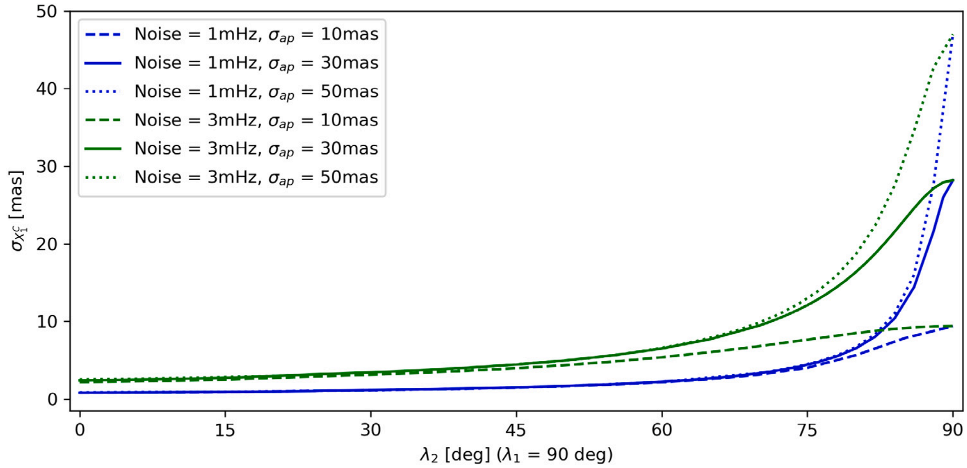

Fig. 13. Influence of the Doppler observable noise on PM determination for the case of the X_1^C term after 700 days. We simulate a range of two-lander scenarios, with both landers placed at latitude $\theta = 20°$, with the longitude of the first lander fixed at $\lambda_1 = 90°$ and the longitude of the second lander λ_2 varied between 0° and 90°. σ_{ap} refers to the *a priori* uncertainty of the estimated terms.

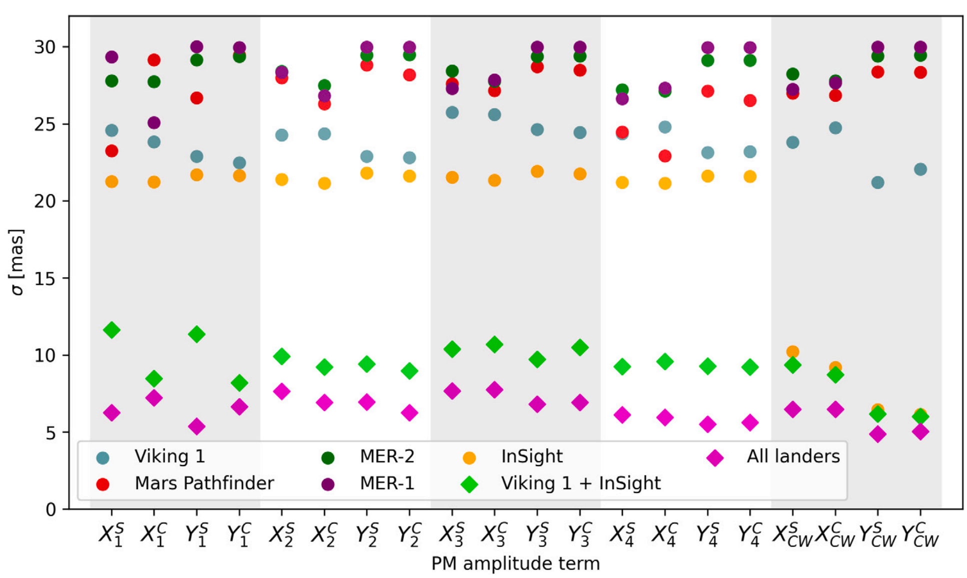

Fig. 14. Comparison of formal errors for solutions using synthetic measurements for combinations of past landers. The circle markers correspond to single-lander datasets, with the diamond markers corresponding to combined datasets. We have removed measurements for which SEP < 15°.

realistic compared to the two-lander one. Moreover, the promising results shown here suggest that a two-lander architecture might be sufficient for improving the Mars rotation models.

5. Conclusions

Despite the success of InSight/RISE in detecting the Free-Core-Nutation mode and refining the rotation and orientation parameters of Mars, more needs to be done to better understand Martian rotational dynamics and further constrain the interior and atmosphere dynamics of the red planet. This article demonstrates the benefit of a second mission performing radio-science from the surface of Mars, in particular to measure its polar motion. We have analysed the possibility of determining the components of the polar motion of Mars with Doppler data from Martian landers. We have proven that it is impossible to determine both X and Y components of the polar motion with a single lander because of large correlations with the spin angle variations. However, with the exclusion of sub-optimal locations, combining Doppler data from two landers enables the decorrelation between the polar motion and spin angle terms, and the simultaneous estimation of all parameters. The relative location of the two landers is identified as the primary driver of the achievable precision of the solution. In particular, longitudinal separation is necessary for the decorrelation of both polar motion components from the spin angle, and allows for full polar motion determination from individually sub-optimal locations. The minimum longitudinal separation required is driven by the latitudes of the landers, with the formal errors decreasing as the latitudinal separation of the landers is increased. A dataset covering a full Martian year or more is required for both landers to reach optimal precision in polar motion estimates and remove the dependence on the *a priori* uncertainty. Furthermore, while the relative timing of the two missions does not significantly influence the theoretical solution without taking into account the effect of mismodelling and bias of other parameters, those effects will have to be considered when analysing data from missions operating at different periods.

We have also compared the results for Doppler observations with those for other radio-science techniques. We have found that, unlike Doppler from two landers, Same-Beam-Interferometry (SBI) by itself is unable to simultaneously resolve the X and Y components of polar motion together with the spin angle variations $\Delta\phi$. This can be mitigated

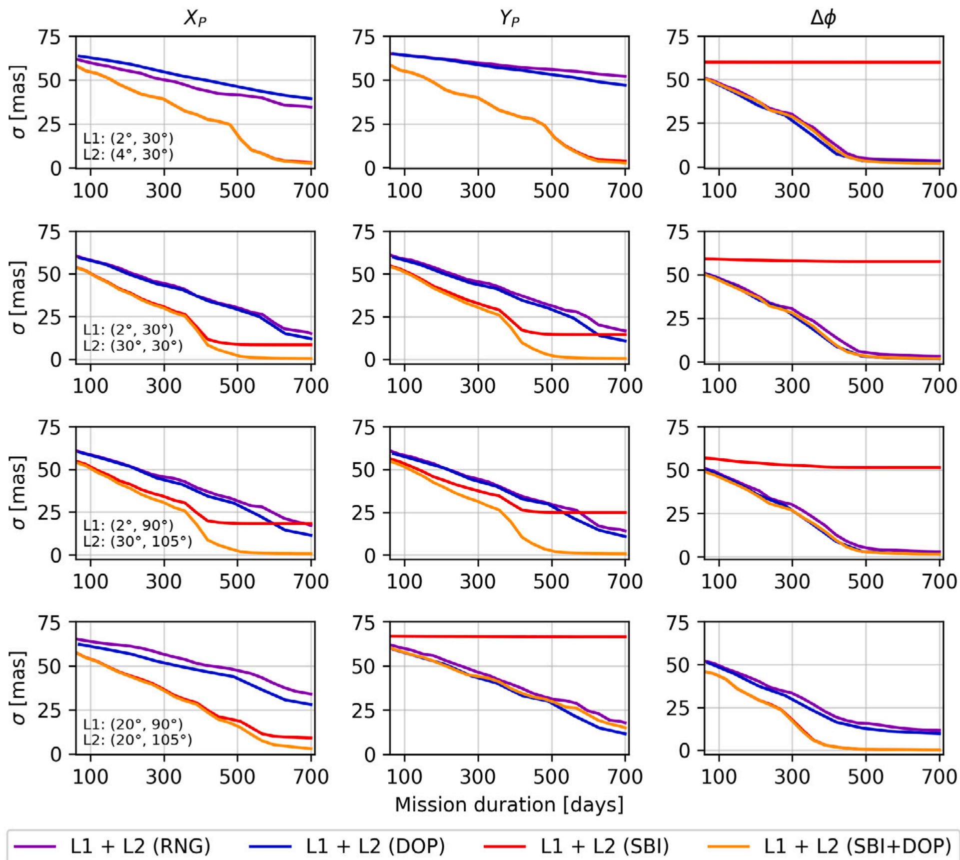

Fig. 15. Comparison of the relative performance of different techniques for different baselines. The cumulative formal errors are plotted.

by combining SBI observables with traditional range or Doppler data, or by utilizing more than two spacecraft. In particular, the formal errors in an estimation combining SBI from two landers with Doppler from one of these landers are equal to or noticeably lower than those using only one technique. Moreover, for most baselines, SBI can reach its final parameter precision after a shorter mission duration than simultaneous range or Doppler tracking from two landers.

Finally, we have conducted preliminary simulations of polar motion determination using synthetic measurements acquired at the same time and with the same noise as the Doppler data from historical missions, showing their theoretical potential to determine the polar motion of Mars. Future work will involve the estimation of polar motion using the actual historical datasets and a full set of fitted parameters.

CRediT authorship contribution statement

Marta Goli: Writing – review & editing, Writing – original draft, Visualization, Validation, Software, Project administration, Methodology, Investigation, Formal analysis, Data curation, Conceptualization. **Sébastien Le Maistre:** Writing – review & editing, Writing – original draft, Validation, Supervision, Project administration, Methodology, Investigation, Funding acquisition, Conceptualization. **Marie Yseboodt:** Writing – review & editing, Writing – original draft, Validation, Software, Methodology, Investigation, Formal analysis, Conceptualization.

Declaration of competing interest

The authors declare that they have no known competing financial interests or personal relationships that could have appeared to influence the work reported in this paper.

Data availability

No data was used for the research described in the article.

Acknowledgements

This work was financially supported by the Belgian PRODEX program managed by the European Space Agency in collaboration with the Belgian Federal Science Policy Office. We thank Alfonso Caldiero for his contribution to the MONTE code development at the ROB and Tim van Hoolst for discussion regarding polar motion and gravity modelling.

Appendix. Analytical equations and the covariance analysis

If the model is linear in the parameters vector $\mathbf{m}$, the data vector $\mathbf{d}$ can be expressed as

$$\mathbf{d} = \mathbf{G}\,\mathbf{m} \tag{13}$$

where $\mathbf{G}$ is the linear model (see for example Tarantola, 2005). Each element $\mathbf{G}_{ij}$ is the derivative of the observable with respect to the model parameter p_j, evaluated at the observation time t_i. Then the *a posteriori* variance–covariance matrix of the least-squares inverse problem $\tilde{\mathbf{C}_M}$ is given by

$$\tilde{\mathbf{C}_M} = \left(\mathbf{G}^T\,\mathbf{C}_\mathbf{D}^{-1}\,\mathbf{G} + \mathbf{C}_\mathbf{M}^{-1}\right)^{-1} \tag{14}$$

$\mathbf{C}_\mathbf{D}$ is the *a priori* covariance matrix of the data. We assume here that the data are uncorrelated and that the data noise level is constant, leading to $\mathbf{C}_\mathbf{D} = 1/\sigma^2_{Dop}\,\mathbf{I}$, $\mathbf{I}$ being the identity matrix.

$\mathbf{C}_\mathbf{M}$ is the *a priori* covariance matrix of the model and the parameters. Again, we assume here that all the non-diagonal elements of this matrix are null and all the diagonal elements (the squared *a priori* uncertainty on the rotation and orientation parameters σ_{ap}) are equal ($\mathbf{C_M} = 1/\sigma_{ap}^2\, \mathbf{I}$).

If this method is applied to the Doppler observable for a rotation model with 3 parameters (X_1^C, Y_1^C and ϕ_1^C) and **one lander only**, the first step is to compute the partial derivative of the Doppler observable with respect to the amplitudes of the polar motion and spin angle parameters using Eqs. (6) for all the observation times i. The second step is to create the $\mathbf{G}^T\,\mathbf{C_D^{-1}}\,\mathbf{G}$ matrix by summing over the observation times:

$$\mathbf{G}^T\,\mathbf{C_D^{-1}}\,\mathbf{G} = \frac{1}{\sigma_{Dop}^2}\sum_i \begin{pmatrix} \frac{\partial q_i}{\partial X_1^C}^2 & \frac{\partial q_i}{\partial X_1^C}\frac{\partial q_i}{\partial Y_1^C} & \frac{\partial q_i}{\partial X_1^C}\frac{\partial q_i}{\partial \phi_1^C} \\ \frac{\partial q_i}{\partial X_1^C}\frac{\partial q_i}{\partial Y_1^C} & \frac{\partial q_i}{\partial Y_1^C}^2 & \frac{\partial q_i}{\partial Y_1^C}\frac{\partial q_i}{\partial \phi_1^C} \\ \frac{\partial q_i}{\partial X_1^C}\frac{\partial q_i}{\partial \phi_1^C} & \frac{\partial q_i}{\partial Y_1^C}\frac{\partial q_i}{\partial \phi_1^C} & \frac{\partial q_i}{\partial \phi_1^C}^2 \end{pmatrix} \tag{15}$$

For each element of this matrix, we isolate the constant factor, independent of time, and use some trigonometric relations to replace the product of cosines and/or sines by cosines and sines of twice the angle. Everything that now depends on the observation time is in different sums over the observation times. These sums can be classified into 2 categories:

- The sums that contain the diurnal or semi-diurnal angles like $\cos 2H_E(t_i)$ or $\sin 2H_E(t_i)$. If the observations are not all planned at the same local hour, the trigonometric functions oscillate between positive and negative values and the sums are close to zero.
  Those sums include $\Sigma_{C2H} = \sum_i \cos 2H_E(t_i)\cos^2\delta_E(t_i)\cos^2(f_1\, t_i)$ and $\Sigma_{S2H} = \sum_i \sin 2H_E(t_i)\cos^2\delta_E(t_i)\cos^2(f_1\, t_i)$.
- The sums that contain only the long-period motion (like the Earth declination or the annual frequency). Because of the product of derivatives, only squared quantities appear here and the summed quantities will be positive, accumulating every time a new observation is added. Numerically these sums are the largest and increase with time.
  Those sums include $\Sigma_{Cft} = \Sigma_i \cos^2\delta_E(t_i)\cos^2(f_1\, t_i)$ and $\Sigma_{Sft} = \Sigma_i \sin^2\delta_E(t_i)\cos^2(f_1\, t_i)$.

We therefore set the sums in the first category to zero.

After these simplifications, we add $\mathbf{C_M}$ and invert Eq. (15), leading to the variance–covariance matrix. The squared root of the diagonal elements are the *a posteriori* uncertainties (or formal errors) of Eqs. (8).

This process can be applied for the single-lander and two-lander configurations, using the Doppler or the SBI observable. In all cases, we end up with sums of the time-varying terms, and the ones including diurnal periodicities can be neglected with respect to the accumulating sums.

References

Baland, R.-M., Yseboodt, M., Le Maistre, S., Rivoldini, A., Van Hoolst, T., Dehant, V., 2020a. The precession and nutations of a rigid Mars. Celest. Mech. Dyn. Astron. 132 (9).

Baland, R.-M., Yseboodt, M., Le Maistre, S., Rivoldini, A., Van Hoolst, T., Dehant, V., 2020b. The precession and nutations of a rigid Mars. URL https://lara.oma.be/RigidNutations/BMAN20.html.

Bizouard, C., 2020. Geophysical Modelling of the Polar Motion. De Gruyter.

Border, J.S., Folkner, W.M., Kahn, R.D., Zukor, K.S., 1991. Precise tracking of the Magellan and pioneer venus orbiters by same-beam interferometry. Adv. Astronaut. Sci. 75.

Buccino, D., Border, J.S., Folkner, W.M., Kahan, D., Le Maistre, S., 2022. Low-SNR Doppler data processing for the insight radio science experiment. Remote Sens. (ISSN: 2072-4292) 14 (8), 1924. http://dx.doi.org/10.3390/rs14081924, URL https://www.mdpi.com/2072-4292/14/8/1924.

Cazenave, A., Balmino, G., 1981. Meteorological effects on the seasonal variations of the rotation of Mars. Geophys. Res. Lett. 8 (3), http://dx.doi.org/10.1029/GL008i003p00245.

Chao, B.F., Rubincam, D.P., 1990. Variations of Mars gravitational field and rotation due to seasonal CO2 exchange. J. Geophys. Res.: Solid Earth 95.

Defraigne, P., de Viron, O., Dehant, V., Van Hoolst, T., Hourdin, F., 2000. Mars rotation variations induced by atmosphere and ice caps. J. Geophys. Res. 105 (E10), 24563–24570. http://dx.doi.org/10.1029/1999JE001227.

Dehant, V., De Viron, O., Karatekin, O., Van Hoolst, T., 2006. Excitation of Mars polar motion. Astron. Astrophys. 446.

Dehant, V., Le Maistre, S., Baland, R.-M., Bergeot, N., Karatekin, O., Péters, M.-J., Rivoldini, A., Ruiz Lozano, L., Temel, O., Van Hoolst, T., Yseboodt, M., Mitrovic, M., Kosov, A.S., Valenta, V., Thomassen, L., Karki, S., Al Khalifeh, K., Craeye, C., Gurvits, L.I., Marty, J.-C., Asmar, S.W., Folkner, W.M., LaRa Team, 2020. The radioscience LaRa instrument onboard ExoMars 2020 to investigate the rotation and interior of mars. Planet. Space Sci. 180.

Evans, S., Taber, W., Drain, T., Smith, J., Wu, H.-C., Guevara, M., Sunseri, R., Evans, J., 2018. MONTE: The next generation of mission design and navigation software. CEAS Space J. 10, http://dx.doi.org/10.1007/s12567-017-0171-7.

Fienga, A., Deram, P., Ruscio, A.D., Viswanathan, V., Camargo, J.I.B., Bernus, L., Gastineau, M., Laskar, J., 2021. INPOP21a planetary ephemerides.

Folkner, W.M., Border, J.S., 1990. Orbiter-orbiter and orbiter-lander tracking using same-beam interferometry. In: AIAA/AAS Astrodynamics Conference.

Folkner, W.M., Kahn, R.D., Preston, R.A., Yoder, C., 1997. Mars dynamics from Earth-based tracking of the Mars Pathfinder lander. J. Geophys. Res. 102.

Gauchez, D., Souchay, J., 1999. Analysis and comparison of different estimates of Mars' polar motion. Earth Moon Planets 84.

Gregnanin, M., 2014. The Rotation and Solid Tides of Mars from Same Beam Interferometry of a Lander Network (Ph.D. thesis). Sapienza University of Rome.

Hamilton, T., Melbourne, W., 1966. Information content of a single pass of Doppler data from a distant spacecraft. In: JPL Space Programs Summary No 37-39, vol. III, Jet Propulsion Laboratory, pp. 18–23.

Konopliv, A.S., Park, R.S., Rivoldini, A., Baland, R.-M., Le Maistre, S., Van Hoolst, T., Yseboodt, M., Dehant, V., 2020. Detection of the chandler wobble of Mars from orbiting spacecraft. Geophys. Res. Lett. 47 (21), e90568. http://dx.doi.org/10.1029/2020GL090568.

Konopliv, A.S., Yoder, C.F., Standish, E.M., Yuan, D.-N., Sjogren, W.L., 2006. A global solution for the Mars static and seasonal gravity, Mars orientation, Phobos and Deimos masses, and Mars ephemeris. Icarus 182 (1), 23–50. http://dx.doi.org/10.1016/j.icarus.2005.12.025.

Le Maistre, S., 2016. InSight coordinates determination from direct-to-Earth radio-tracking and Mars topography model. Planet. Space Sci. (ISSN: 00320633) 121, 1–9. http://dx.doi.org/10.1016/j.pss.2015.11.003, URL https://linkinghub.elsevier.com/retrieve/pii/S0032063315300532.

Le Maistre, S., Dehant, V., Baland, R.-M., Beuthe, M., Caldiero, A., Filice, V., Goli, M., Péters, M.-J., Steenput, B., Rivoldini, A., Ümit, E., Van Hoolst, T., Yseboodt, M., 2022. LaRa, an X-band coherent transponder ready to fly. In: Europlanet Science Congress 2022. Granada, Spain.

Le Maistre, S., Rivoldini, A., Caldiero, A., Yseboodt, M., Baland, R.-M., Beuthe, M., Van Hoolst, T., Dehant, V., Folkner, W., Buccino, D., Kahan, D., Marty, J.-C., Antonangeli, D., Badro, J., Drilleau, M., Konopliv, A., Péters, M.-J., Plesa, A.-C., Samuel, H., Tosi, N., Wieczorek, M., Lognonné, P., Panning, M., Smrekar, S., Banerdt, B., 2023. Spin state and deep interior structure of Mars from InSight radio tracking. Nature 619, 733–737, doi: s41586-023-06150-0.

Le Maistre, S., Rosenblatt, P., Dehant, V., Marty, J.-C., Yseboodt, M., 2018. Mars rotation determination from a moving rover using Doppler tracking data: What could be done? Planet. Space Sci. 159, http://dx.doi.org/10.1016/j.pss.2018.03.020.

Le Maistre, S., Rosenblatt, P., Rivoldini, A., Dehant, V., Marty, J.-C., Karatekin, O., 2012. Lander radio science experiment with a direct link between Mars and the Earth. Planet. Space Sci. 68.

Montenbruck, O., Gill, E., 2000. Satellite Orbits. Springer Berlin Heidelberg, http://dx.doi.org/10.1007/978-3-642-58351-3.

Park, R.S., Folkner, W.M., Williams, J.G., Boggs, D.H., 2021. The JPL planetary and lunar ephemerides DE440 and DE441. Astron. J. 161 (3), 105. http://dx.doi.org/10.3847/1538-3881/abd414, ISSN: 0004-6256, 1538-3881URL https://iopscience.iop.org/article/10.3847/1538-3881/abd414.

Péters, M.-J., Le Maistre, S., Yseboodt, M., Marty, J.-C., Rivoldini, A., Van Hoolst, T., Dehant, V., 2020. LaRa after RISE: Expected improvement in the Mars rotation and interior models. Planet. Space Sci. 180, 104745. http://dx.doi.org/10.1016/j.pss.2019.104745.

Tarantola, A., 2005. Inverse Problem Theory and Methods for Model Parameter Estimation. Society for Industrial and Applied Mathematics, http://dx.doi.org/10.1137/1.9780898717921, URL https://epubs.siam.org/doi/abs/10.1137/1.9780898717921.

Van Den Acker, E., Van Hoolst, T., De Viron, O., Defraigne, P., Forget, F., Hourdin, F., Dehant, V., 2002. Influence of the seasonal winds and the CO2 mass exchange between atmosphere and polar caps on Mars' rotation. J. Geophys. Res.: Planets 107, http://dx.doi.org/10.1029/2000JE001539.

Van Hoolst, T., Dehant, V., Defraigne, P., 2000. Chandler wobble and free core nutation for Mars. Planet. Space Sci. 48 (12–14).

Yoder, C.F., Standish, E.M., 1997. Martian precession and rotation from Viking lander range data. J. Geophys. Res.: Planets http://dx.doi.org/10.1029/96JE03642.

Yseboodt, M., Baland, R.-M., Le Maistre, S., 2023. Mars orientation and rotation angles. Celest. Mech. Dyn. Astron. 135 (5), 50. http://dx.doi.org/10.1007/s10569-023-10159-y.

Yseboodt, M., Barriot, J.-P., Dehant, V., 2003. Analytical modeling of the Doppler tracking between a lander and a Mars orbiter in terms of rotational dynamics. J. Geophys. Res.: Planets 108.

Yseboodt, M., Dehant, V., Péters, M.-J., 2017. Signatures of the Martian rotation parameters in the Doppler and range observables. Planet. Space Sci. 144, 74–88. http://dx.doi.org/10.1016/j.pss.2017.05.008.